RSC Advances

ROYAL SOCIETY OF CHEMISTRY

www.rsc.org/advances

Cite this: DOI: 10.1039/c0xx00000x

www.rsc.org/xxxxxx

ARTICLE TYPE

2D Hybrid anode based on SnS Nanosheet bonded with graphene to Enhance Electrochemical Performance for Lithium-Ion Batteries

Shuankui Li,[a,b] Jiaxin Zheng [b], Shiyong Zuo,[a] Zhiguo Wu,[a] Pengxun Yan [a], and Feng Pan*[b]*

Received (in XXX, XXX) Xth XXXXXXXXX 20XX, Accepted Xth XXXXXXXXX 20XX

DOI: 10.1039

Hybrid anode based on SnS nanosheet bonded with graphene synthesized by reduced graphene oxide (SnS NS/RGO) is formed through a facile solvothermal method. It is found that the 2D SnS nanosheets with few layers are well dispersed on the crumpled reduced graphene oxide surface. Electrochemical tests indicate that the SnS NS/RGO hybrid exhibit a very high reversible capacity (791mAhg^{-1}) with excellent cycle stability and significantly enhanced rate capability. The factors contributing to the enhanced electrochemical performance of the hybrid cathode can be ascribed to the chemical bonded interface between SnS NS and RGO to create effective charge transportation with the electron coupling in the novel two-dimensional composite nanostructure. This work provides the insights for the structural design of SnS-based hybrid electrodes materials, which will be important for future development of high performance electrode materials.

Introduction

Li-ion batteries (LIBs) are the most used renewable energy sources for all kinds of portable electronic device owing to its excellent energy conversion efficiency and high energy density.[1-5] However, the anode material in the commercially available Li-ion batteries is typically graphite, which exhibits a low theoretical lithium storage capacity of around 370mAhg^{-1} and poor rate capability.[6-8] To meet the continuous demands for electrochemical energy storage, high performance electrode materials for the next generation of LIB, especially the anode materials, such as Si, [9] tin-based compound, [10] and metal oxides[11]have been under intense research during the past decade. Tin-based compound is one of promising anode material for lithium ion batteries due to its low cost, high theoretical capacity, and wide spread availability. Stannous sulfide (SnS) is an important tin-based compound with a high theoretical capacity (782mAhg^{-1} based on 4.4Li per molecular), which is considered as a particularly interesting anode material for LIBs. However, the practical application of the SnS anode is still a challenge due to its poor electron transport, slow Li-ion diffusion in electrodes, which leads to poor cycling and rate performance. [12-14] Various SnS nanostructures, such as 1D nanowires, 2D nanosheets, [15, 17] and 3D SnS nanoflowers, [13] has been extensively studied in order to improve electrochemical performance by shortening Li-ion and electron diffusion path, enlarging electrode/electrolyte interfacial area as well as facilitating strain relaxation during the insertion/extraction processes. However, the electrochemical performance of these SnS is still limited by its extremely low electrical conductivity. The design and fabrication of SnS based electrodes with the high specific capacity and high-rate capability is still a great challenge. [18, 19]

Combination of SnS with conducting agents to form SnS-based hybrids, have been regarded as one of effective approach to circumvent the above issues. [20, 21] Graphene, a new 2D carbon material, is considered as an ideal matrix to support 2D SnS nanosheets, not only due to its appealing characteristics such as large specific surface area, superior electronic conductivity, and excellent structural flexibility, but also due to its 2D layered structure which benefits for forming well aligned layered composites.[22] In our previous work, we found the depolarization effect of the hybrid electrode with cathode (such as Li_2FeSiO_4 (LFS)) chemically bonded to graphene, due to the electron coupling at the interface between cathode (nano-LFS) and graphene to create effective charge transportation so as to improves the electrochemical performance.[23] Consequently, modification of SnS anode material with graphene has attracted broad interest, which expected to largely enhance its electrochemical performance. The synergy between the functions of the two materials, high capacity of SnS and good electronic conductivity of graphene to generate the high lithium ions diffusion efficiency can be exploited in the SnS nanosheet/graphene hybrids to yield high performance anodes in Li-ion batteries.[12] However, very few reports study the electrochemical performance of the uniform 2D SnS nanosheet to chemically bond with graphene as the hybrid anode material for lithium ion batteries.

Herein, we report a facile solvothermal method to grow SnS nanosheet (NS) on reduced graphene oxide (RGO) nanosheet to form SnS NS/RGO hybrids. The as-prepared hybrid exhibits a very high reversible capacity (as high as 791mAhg^{-1}) with the excellent cycle stability and good rate capability. The well aligned layered structures for the hybrid SnS NS/RGO hybrids and the well coupled interface between SnS NS and graphene ensure the synergy between the functions of the two materials, high capacity of SnS and good electronic conductivity of graphene, thus yielding the high electrochemical performance.batteries.

Experimental Section

Preparation of SnS NS/RGO hybrid: Natural graphite powder was oxidized to graphite oxide (GO) by the modified Hummers'

method. The SnS NS/RGO hybrid was prepared by a solvothermal route. In a typical synthesis of SnS NSs/RGO hybrid, 20mg of graphite oxide were dispersed into 30ml ethylene glycol solution by ultra-sonication for 60 min. Then, 226mg $SnCl_2.2H_2O$ (1 mmol), 210mg citric acid were added to the solution and then stirring for 60 min. 2ml $(NH_3)_2S$ was added to the solution and the final solution was further stirred for 5min, and then transferred to a 40 mL Teflon-lined stainless steel autoclave. After heating at 190 °C for 18h then naturally cooling to room temperature, the black products ware filtered and washed several times with deionized water and absolute ethanol, and dried at 60 °C for 24h to obtain the two-dimensional (2D) hybrid SnS nanosheet/reduced graphene oxide. The pure SnS was fabricated without the graphite oxide as comparison.

Electrochemical measurements: CR2016 type half cells were assembled with the prepared hybrids as the anode material in a high-purity argon-filled glove box. The anodes were prepared by mixing active materials, carbon black, and polyvinylidene difluoride (PVDF) at a weight ratio of 80:10:10 in NMP (N-methyl-2-pyrrolidone) solvent to form slurry. The typical loading density on a Cu foil was ~1.5 mg/cm^2. A Li foil was used as the cathode. $LiPF_6$ (1M) in ethylene carbonate (EC)/diethyl carbonate (DEC) (1:1 w/w) was used as the electrolyte. The charge/discharge tests were performed on a multi-channel battery workstation (LAND-CT2001C). Cyclic voltammetry (CV) and electrochemical impedance spectroscopy (EIS) was performed on a CHI660E electrochemical workstation.

Characterization: The morphology and structure were observed by scanning electron microscopy (SEM, Hitachi S-4800) with an acceleration voltage of 5kV, transmission electron microscopy (TEM: JEM-2100) operated at 200kV. The crystal structures of the as-synthesized products were characterized by X-ray diffraction (XRD) on a Philips X'Pert Pro Diffractometer, using Cuα1 radiation (λ=1.54056Å). The X-ray photoelectron spectroscopy (XPS) data were determined on Thermo Scientific XPS spectrometers.

Results and Discussion

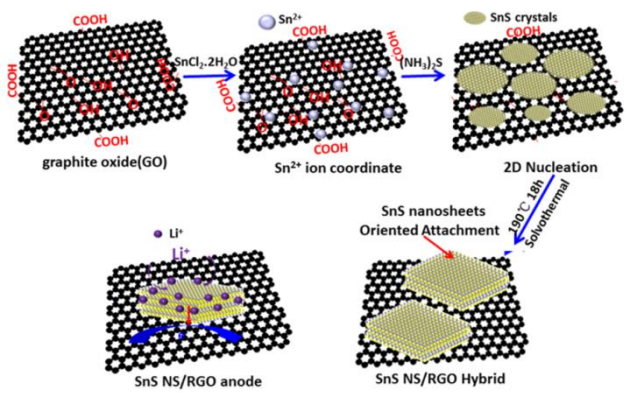

Schematic 1. Schematic diagram of the SnS NS/RGO hybrid.

The fabrication process of the SnS NS/RGO is illustrated in Scheme.1. At the early stage, Sn^{2+} ion can be very easily absorbed on the GO by the coordinate interaction between the oxygen-containing functional groups (-OH and –COOH) on GO and Sn^{2+} ion to generate the chemical bonds. Therefore, as the $(NH_3)_2S$ was added to the solution, the nucleation and subsequent growth of SnS is selective on GO surfaces with little free particle growth in solution. Subsequently, under the solvothermal condition, SnS crystals are grown according to its growing habit to further reduce the interface energy between primary nanoparticles. In the case of the orthorhombic structure of SnS, the (100) facets are the most stable facets due to the strongest ionic interactions. Accordingly, it is rational that the SnS nanostructure tends to expose (100) facets. The 2-dimension nucleation and growth of SnS on the GO surfaces lead to the formation of SnS NS/RGO hybrid. It should be pointed out that the initial GO will be reduced under the solvothermal condition.[24] The structured SnS NS/RGO hybrid electrode is designed with the following advantages: (1) ultrathin plate-like SnS subunits to facilitate fast Li^+ diffusion and alleviate the pulverization, (2) highly conductive RGO framework to enhance electronic conductivity of the electrode, (3) the well aligned layered structures and the well coupled interface between SnS NS and graphene are beneficial to the effectively and rapidly charge transfer from ultrathin SnS layers to graphene layers, (4) large surface area of RGO framework to improve electrolyte wettability and relieve the mechanical stress and accommodate large volume change. [25]

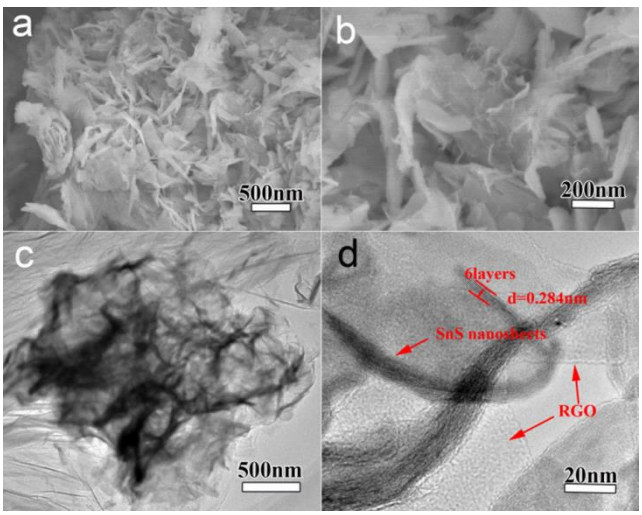

Figure 1. SEM and HRTEM images of the as-synthesized SnS NS/RGO(D10). (a) and (b) SEM images. (c) and (d) TEM images.

The morphology and microstructure of the as-prepared SnS NS/RGO hybrid ware studied by field emission scanning electron microscopy (SEM) and transmission electron microscopy (TEM). The SEM image in Fig.1a reveals the 2D morphology of SnS NS/RGO(D10) hybrid. Abundant irregular SnS nanosheets with the thickness of about 10-20 nm are clearly observed in the SEM image. It is should be noted that the SnS nanosheets (Fig.1b) are more rigid and thicker than the graphene nanosheets. The TEM image in Fig. 1c further clearly shows the curved SnS nanosheets dispersed on the large RGO substrates, indicating the formation of a hybrid SnS nanosheet-RGO heterostructure. Furthermore, the as-prepared SnS NS/RGO(D10) architecture possesses a hybrid structure with interconnected pores, which can effectively accommodate the large volume change, thus leading to improved lithium-storage properties. As shown in Fig.1d, the SnS shows a well-layered structure interaction with an interlayer distance of the (400) plane of 0.28nm supports on graphene surface. It is well known that the orthorhombic SnS phase has a layered structure

along the b-axis. The bonding within the layer is dominated by covalent bonding between Sn and S atoms, while the bonding between the layers, separated by 2.668Å, is maintained by the weak vander Waals force. The thickness of the nanosheets is about 5-10nm; this indicates that each sheet is composed of 20-40 layers of SnS along the b-axis. Owing to this weakly bound interlayer characteristic, the attachment of atoms on the lattice along the b-axis, during synthesis, generates such a high free energy that the crystal growth along this direction proceeds slowly, leading to the formation of anisotropic 2D nanosheets.[24] The partial overlapping or coalescing of flexible nanosheets is likely to be originated from the cross-linking of the functional groups in the graphene sheets, and thus, the SnS nanosheets are much easier to efficiently combine with graphene.

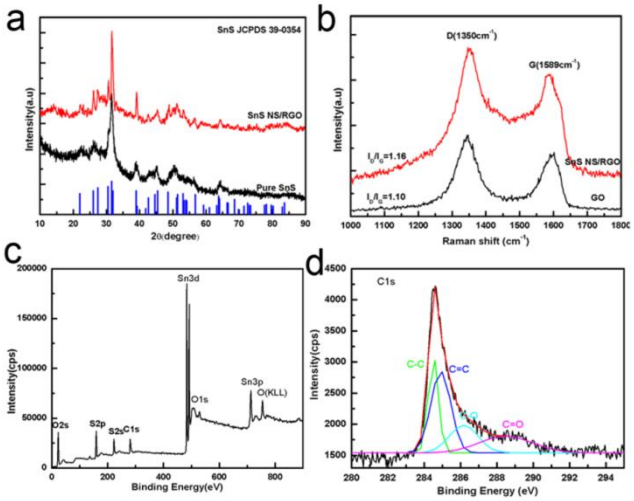

Figure 2. (a) XRD curves and (b) Raman spectrum of the SnS NS/RGO composite. XPS spectra of SnS NS/RGO hybrid: (c) survey; (d) C 1s.

Fig.2a shows the XRD patterns of the hybrid SnS NSs/RGO (D10)and bare SnS. The diffract gram of SnS also matched well with the reported JCPDS data of orthorhombic SnS (Space group: Pbnm, JCPDS 39-0354) with lattice constants of a=4.3291Å, b=11.1923Å, and c=3.9838Å. Because of the low amount and the relatively low diffraction intensity of RGO in the composites, no characteristic diffraction of carbon species can be observed after the introduction of GO. Fig.2b compares the Raman spectra of SnS NS/RGO(D10) and GO, two typical carbon peaks are observed. The peak at about 1589 cm^{-1} (G band) is related to the vibration of the sp^2-bonded carbon atoms in a 2-dimensional hexagonal lattice, while the peak at about 1326 cm^{-1} (D band) is related to the defects and disorder in hexagonal graphitic layers. The intensity ratio of the D band to G band (I_D/I_G) of SnS NS/RGO is calculated as 1.16, which is higher than those of GO. The slightly enhancement of the intensity ratio in the SnS NS/RGO(D10) can be attributed to the increase of the disorder in the GO resulting from aggressive solvothermal reaction and the SnS nanosheets loading.

To further evaluate the SnS NS/RGO(D10) composite, X-ray photoelectron spectroscopy (XPS) was measured, as shown in Fig.2c. The two strong peaks at around 486.8 and 495.4 eV (Fig.S1c) can be attributed to Sn $3d_{5/2}$ and $3d_{3/2}$ respectively, which agrees well with the reference data of Sn^{2+} in SnS. No evidence of Sn^{4+} (binding energy at 485.9eV) was detected in the spectra. The $S2p_{3/2}$ at 161.83 eV (Fig.S1d) and $S2s_{1/2}$ at 223.51 eV are attributed to binding energies of SnS, which demonstrates that there is no elemental sulfur (164.05 eV in binding energy) contained in the sample.[26] The C 1s peak (284.5 eV) corresponds to the C-C bonding (sp^2 carbon) in graphite is much strong. The peak arising from the oxygenated carbons (carbon in C−O at 286.2 eV; carbonyl carbon, C=O, 287.9eV) is also observed, suggesting that the oxygen-containing (C-O, C=O) functional groups on the surfaces of the GO to chemically bonding with Sn of SnS to generate the interfacial bonding (-C-O-Sn-) as shown in Fig.2d. Under the solvothermal condition, the increased temperature and autogenous pressure lead to the reduction of graphene oxide into RGO, but the C-O or C=O of interfacial bonding (-C-O-Sn-) will be still left during the reduction .

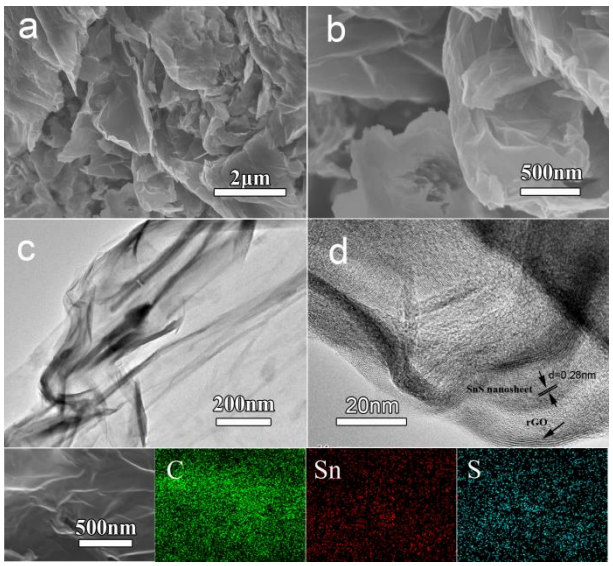

Figure 3. SEM and HRTEM images of the as-synthesized SnS NS/RGO (L5) fabricated under the low concentration of Sn^{2+} source (the amount of $SnCl_2.2H_2O$ reduced to 0.5mmol). (a) and (b) SEM images. (c) and (d) TEM images. (f) EDX mapping images of Sn, S, and C elements.

To compare with the SnS NS/RGO, the pure SnS prepared without the graphite oxide has similar morphology. As shown in Fig.S2, many irregular nanosheets with a thickness of about 10nm are clearly observed. Another kind of SnS NS/RGO composites (SnS NS/RGO(L5)) fabricated under the low concentration of Sn^{2+} source (the amount of $SnCl_2.2H_2O$ is reduced to 0.5mmol), is shown in Fig.3. The composites also deliver a 2-dimensional nanoflake structure (Fig.3a-c). The high-resolution TEM (HRTEM) image shows that SnS layers with an interlayer distance of 0.28nm are grown on the surface of graphene (Fig. 3d) and the thickness of SnS (about 4-5 layers) grown on the surface of graphene is quite thinner than that of SnS NS/RGO(D10). To verify the 2-dimensional nanoflake structure that SnS layers grown on the surface of graphene, EDX elemental mappings (Fig.3) of the nanosheet were obtained. The result clearly indicates that there is a uniform dispersion of the element C, Sn, S in the nanosheet. The carbon contents of SnS NS/RGO (D10) and (L5) determined by thermogravimetric analysis (TGA) (Fig.S3) are 17.9 and 44.6wt%, respectively, indicating the latter sample with higher loading ratio of SnS nanosheets on the RGO

surfaces.

It is well known that the lithium intercalation and conversion reactions of Sn-based anode material based on the formation of metallic Sn and subsequent generation of a Li-Sn alloy: [27]

$SnS + xLi^+ + xe^- \rightarrow Li_2S + Sn$ (1)

$Sn + xLi^+ + xe^- \leftrightarrow Li_xSn\ (0 \leqslant x \leqslant 4.4)$ (2)

Cyclic voltammetric (CV) experiments was carried out to understand the electrochemical reactive process of the the SnS/RGO hybrids in the range of 0.02-1.5V for five cycles at a scan rate of $0.2mVs^{-1}$. The broad peak located at around 1V in the first cathodic scan corresponds to the reduction of SnS to metallic Sn accompanying the formation of Li_2S and the solid electrolyte interphase (SEI) film, as shown in Eq.(1), and similar results have previously been reported for other Sn-based anode material.[26, 27] The decomposition of the SnS into metallic Sn and Li_2S as well as the formation of solid electrolyte interface (SEI) may lead to the large irreversibility of SnS-based anodes at the first charge/discharge cycle, which is generally consistent with those reported in literature. The more cathodic potential at around 0.23V and the anodic potential at about 0.5V in the first scan can be attributed to the alloying (cathodic scan) and dealloying (anodic scan) processes. From the second cycle onwards, the CV curves mostly overlap, indicating the good reversibility of the electrochemical reactions. In agreement with this CV result, two poorly defined plateaus can be identified in the discharge voltage profiles (Fig.4b).[27]

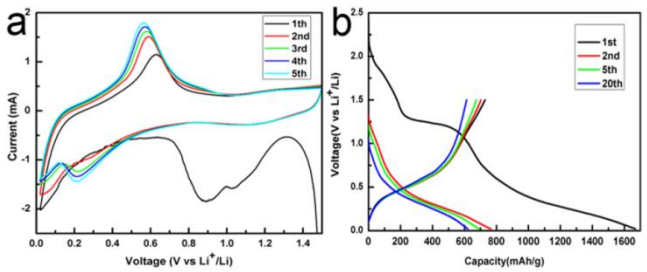

Figure 4. (a) Cycle voltammogram of the SnS NS/RGO S1 electrode at a scan rate of $0.2mVs^{-1}$. (b) The 1st, 2nd, 5th and 20th discharge/charge profiles at a current density of $100mAg^{-1}$.

Benefitted from the unique 2D hybrid structure and the presence of RGO, the SnS NS/RGO exhibits higher rate performance than pure SnS nanosheet. For the SnS NS/RGO(D10) with about 10nm thickness of SnS, when the current densities increase from 100 to 200, 500 and 1000 mAg^{-1}, the electrode exhibits high capacity retention, as the specific capacities change from 785 to 627, 477, and $331mAhg^{-1}$, respectively. Remarkably, when the current rate is reduced back to $100mAg^{-1}$ after 50 cycles, a stable high discharge capacity of about $595mAhg^{-1}$ can be recovered,, indicating the high rate capability and good cycling stability of SnS NS/RGO as anode materials. In addition, it is noteworthy that at a higher current density of 1000 mAg^{-1}, the SnS NS/RGO(L5) with about 4-5 layers SnS was still able to deliver a discharge capacity of $360mAhg^{-1}$, which is much higher than that of SnS NS/RGO(D10) with about 20-30 layers SnS. This might arise from the difference of the RGO content of the 2D hybrid and the thinner layer for SnS. The large content of graphene not only benefits for the electronic transportation, but also can accommodate the large volume change. Furthermore, electrochemical impedance spectroscopy (EIS) measurements were carried out for SnS NS/RGO (D10) and pure SnS electrodes after several cycles in the Nyquist plot (Fig.5d). The values of R_f and R_{ct} of the SnS NS/RGO(D10) hybrids (65Ω, 83Ω) is much lower than pure SnS (69Ω, 174Ω), indicating that charge carriers could be effectively and rapidly conducted back and forth from ultrathin SnS layers to graphene layers. This can be attributed to that the well electron coupling between SnS NS and graphene (Fig.5c) makes SnS NS feel direct electric-potential without IR (current-resistant) deduction to create the depolarization effect to enhance the electrochemical activity of SnS NS. As a result, charge carriers could be effectively and rapidly transport back and forth from SnS layers to graphene layers.

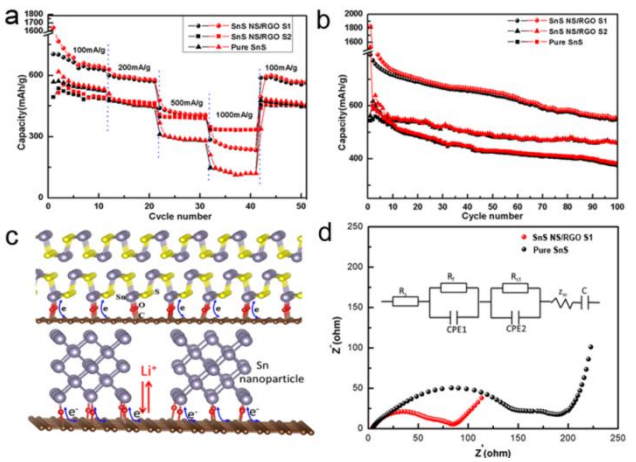

Figure 5. (a) Rate performance of the SnS NS/RGO hybrids at different current densities. (b) Cyclic performance of the SnS NS/RGO hybrids at a current density of $100mAg^{-1}$ for 100 cycles. (c) Schematic diagram of electron coupling between SnS NS and graphene. (d)EIS plots of SnS NS/RGO and SnS electrodes over the frequency range 100 kHz-0.1 Hz after 5 cycles by CV measurement at $0.2mVs^{-1}$.

Fig.5b shows the discharge-charge cycling performance of the above mentioned anode materials evaluated between 0.05 and 1.5 V at a current density of $100mAg^{-1}$. The SnS NS/RGO (D10) and (L5) exhibit very high initial capacity of 1625 and $1535mAhg^{-1}$, respectively. This high initial capacity may be partly attributed to both the presence of defects in the graphene and the disorder of the unique 2D structure of SnS. The initial discharge capacities of SnS NS/RGO (D10) and SnS NS/RGO (L5) were 791 and $601mAhg^{-1}$, which is close to the theoretical specific capacity of SnS ($790mAhg^{-1}$). The irreversible capacity loss may be mainly attributed to irreversible reaction in Eq.(1) and the inevitable formation of solid electrolyte interface (SEI) film, which are common to most Sn-based anode materials. After 100 cycles, the capacities of SnS NS/RGO (D10) and (L5) are stable at about 560 and $460mAhg^{-1}$, delivering 73.7% and 76.5% of the second cycle capacity (791 and $601mAhg^{-1}$) (Fig.5b). Whereas for the pure SnS nanosheet, the capacity decays much faster to less than $400mAhg^{-1}$ within 100 cycles, which could be ascribe to the morphology were inevitably damaged and resulted in aggregation and pulverization after a long time cycling. It should be noted that compared with SnS NS/RGO (D10), the (L5) has a lower capacity but better cyclic performance, which could be mainly attributed to the difference of the RGO content (17.9 and 44.6wt% for S1 and S2). Remarkably, the sample of the SnS NS/RGO (D10) even demonstrates excellent cyclic capacity

retention at higher current rate (Fig. S4). At the end of 100 charge-discharge cycles, a reversible capacity of 520 and 390mAhg^{-1} can be retained at current density of 200 and 500mAg^{-1}, indicating the high rate capability and good cycling stability of SnS NS/RGO as anode materials.

Compared with the previous results for SnS based materials as anodes for LIBs, excellent electrochemical performance of the 2D hybrid SnS nanosheet/reduced graphene oxide electrode provided great potential as high-performance electrode materials for lithium-ion batteries, as shown in Table S1. The excellent cycling stability and rate capability of the SnS NS/RGO hybrids could be attributed to the synergy between the functions of the two materials and the novel two-dimensional composite nanostructure. First, the highly conductive graphene supplies 2D electronically conducting networks for the SnS NS/RGO composites to facilitate the charge transfer. Second, depolarization effect induced by the well electron coupling between SnS NS and graphene makes the SnS NS electrochemically full active.[28] Third, the large surface area of ultrathin SnS subunits with a preferential a-axis orientation lead to more reactive sites and the large contact area between the electrode material and electrolyte, which finally endows the composite with high specific capacity.[29] Finally, the highly conductive and flexible RGO can effectively accommodate the large volume change.

Conclusion

In summary, we have successfully fabricated SnS NS/RGO hybrids by directly growing ultrathin SnS nanosheets onto the GO then to reduce to RGO via a facile solvothermal process. The SnS NS/RGO hybrids exhibits an higher lithium storage capacities and better cycling performance compared to bare SnS due to the rational design and engineering of the unique nanostructure and composition. The unique ultrathin sheet-on-sheet nanostructure not only offers 2D conducting networks but also facilitates the rapid Li-ion transport, leading to enhanced rate capability. The present results suggest that the SnS NS/RGO hybrids can be used as a promising anode material for high performance Li-ion battery.

Acknowledgements

The research was financially supported by Guangdong Innovation Team Project (No. 2013N080), Shenzhen Science and Technology Research Grant (No. ZDSY20130331145131323, CXZZ20120829172325895, JCYJ20120614150338154), and the National Natural Science Foundation of China(No. 11204114).

Notes and references

[a] *School of Physical Science and Technology, Lanzhou University, Lanzhou City, Gansu Province, 730000, China. Tel: 86-931-8912719; E-mail: zgwu@lzu.edu.cn.*

[b] *School of Advanced Materials, Peking University Shenzhen Graduate School, Shenzhen 518055, China Tel: 86-755-26033200; E-mail: panfeng@pkusz.edu.cn.*

1. A.S. Arico, P. Bruce, B. Scrosati, J.-M. Tarascon and W. van Schalkwijk, *Nat. Mater.*, 2005, **4**, 366.
2. N. Kamaya, K. Homma, Y. Yamakawa, M. Hirayama, R. Kanno, M. Yonemura, T. Kamiyama, Y. Kato, S. Hama, K. Kawamoto, A. Mitsui, *Nat. Mater.*, 2011, **10**, 682-686.
3. Y. Idota, T. Kubota, A. Matsufuji, Y. Maekawa, T. Miyasaka, *Science*, 1997, **276**, 1395-1399.
4. M. G. Kim and J. Cho, *Adv Funct Mater*, 2009, **19**, 1497-1514
5. M. Armand, J.-M. Tarascon, *Nature*, 2008, **451**,652-657.
6. J. M. Tarascon and M. Armand, *Nature*, 2001, **414**, 359-367.
7. Z.S. Wu, W.C. Ren, L. Wen, L.B. Gao, J.P. Zhao, Z.P. Chen, G. M. Zhou, F. Li, H.M. Cheng, *ACS Nano.*, 2010, **4**, 3187-3194.
8. X.Y. Han, G.Y. Qing, J.T. Sun, T.L. Sun, *Angew. Chem. Int. Ed.*, 2012, **51**, 1-6.
9. K. Fu, O. Yildiz, H. Bhanushali, Y.X. Wang, K. Stano, L.G. Xue, X.W. Zhang, P. D. Bradford, *Adv. Mater.*, 2013, **25**, 5109–5114.
10. C.-M. Wang, W. Xu, J. Liu, J.-G. Zhang, L. V. Saraf, B. W. Arey, D. Choi, Z.-G. Yang, J. Xiao, S. Thevuthasan, D. R. Baer, *Nano Lett.*, 2011, **11**, 1874-1880.
11. L. Chen, H.Y. Xu, L. Li, F.F. Wu, J. Yang, Y.T. Qian, *J. Power Sources*, 2014, **245**, 429-435.
12. S.K. Li, S.Y. Zuo, Z.G. Wu, Y. Liu, R.F. Zhuo, J.J. Feng, D. Yan, J. Wang, P.X. Yan, *Electrochimica Acta*, 2014, **1**, 355–362.
13. D.D. Vaughn II, O.D. Hentz, S. Chen,D. Wang, R.E. Schaak, *Chem. Commun.*, 2012, **48**, 5608-5610.
14. Y.J. Zhang, J. Lu, S.L. Shen,H.R. Xu, Q.B. Wang, *Chem. Commun.*, 2011, **47**, 5226-5228.
15. J. Lu, C.Y. Nan, L.H. Li, Q. Peng, Y.D. Li, *Nano Research*, 2013, **6(1)**, 55-64.
16. G.G. Kumar, K. Reddy, K.S. Nahma, N. Angulakshmi, A.M. Stephan, *J. Phys. Chem. Sol.*, 2012, **73**, 1187-1190.
17. J.-G. Kang, J.-G. Park, D.-W. Kim, *Electrochem. Commun.*, 2010, **12**, 307-310.
18. H.C. Tao, X.L. Yang, L.L. Zhang, S.B. Ni, *Journal of Electroanalytical Chemistry*, 2014, **728**, 134–139.
19. J.S. Zhu, D.L. Wang, T.F. Liu, *Ionics*, 2014, **20**, 141–144.
20. D.B. Kong, H.Y. He, Q. Song, B. Wang, Q.H. Yang, L.J. Zhi, *RSC Adv.*, 2014, **4**, 23372-23376.
21. C. Zhai, N. Du and H. Z. D. Yang, *Chem. Commun.*, 2011, **47**, 1270-1272
22. F. Bonaccorso, L. Colombo, G. Yu, M. Stoller, V. Tozzini, A.C. Ferrari, V. Pellegrini, *Science*, 2015, **347(6217)**, 1246501.
23. J.L. Yang, L. Hu, J.X. Zheng, D.P. He, L.L. Tian, S.C. Mu, F. Pan, *J. Mater. Chem. A*, 2015, **3**, 9601-9608.
24. E.M. Lotfabad, J. Ding, K. Cui, A. Kohandehghan, W.P. Kalisvaart, M. Hazelton, D. Mitlin , *ACS Nano.*, 2014, **8**, 7115-7129 .
25. J. Wang, J.L. Liu, D.L. Chao, J.X. Yan , J.Y. Lin, Z. X. Shen, *Adv. Mater.*, 2013, **26(42)**, 7162-7169.
26. P. Jain, P. Arun, *J. Appl. Phys.*, 2014, **115**, 204512.
27. H.B. Wu, J.S. Chen, H.H. Hng, X.W. Lou, *Nanoscale*, 2012, **4**, 2526-2542.
28. G.M. Zhou, L. Li, Q. Zhang, N. Li, F. Li, *Phys. Chem. Chem. Phys.*, 2013, **15**, 5582-5587.
29. X. Huang , C.L. Tan , Z.Y. Yin, H. Zhang, *Adv. Mater.*, 2014, **26(14)**, 2185-2204.